Table 1. NMR and Structure Refinement Statistics for E4B (aa 1208–1302)

Number of restraints	
Total NOE restraints	1368
Intraresidue	64
Sequential ($\|i-j\|=1$)	384
Medium-range ($1<\|i-j\|<4$)	409
Long-range ($\|i-j\|>4$)	511
Hydrogen-bond restraints	36
Dihedral-angle restraints	
Φ	23
Ψ	23
Structure statistics[a]	
Violations (mean ± standard deviation)	
NOE restraints (Å)	0.005 ± 0.001
Dihedral-angle restraints (°)	0.059 ± 0.045
Rmsds from idealized geometry	
Bond lengths (Å)	0.0011
Bond angles (°)	0.396
Improper torsions (°)	0.251
Final energies (kcal·mol^{-1})	
Total	85.0 ± 2.7
Bonds	1.9 ± 0.2
Angles	70.3 ± 1.5
van der Waals	3.2 ± 0.7
NOEs	1.7 ± 0.6
Coordinate precision (Å)[b]	
Rmsds	
Backbone atoms (aa 1228–1295)	0.62
Backbone in secondary structures	0.48
Heavy atoms (aa 1228–1295)	1.17
Heavy atoms in secondary structures	1.07
Ramachandran plot	
Preferred regions (%)	59.1 ± 5.9
Allowed regions (%)	40.0 ± 5.5
Outliers (%)	0.9 ± 1.2

[a] Structure statistics refer to an ensemble of 20 structures with lowest energies from 100 calculated structures.
[b] Average pairwise rmsd for the ensemble of 20 structures.

Table 2. Crystallography Statistics

	E4B U Box	Ubc4	E4B U Box–UbcH5c
Data Collection			
Space group	P432	$P12_11$	P622
Cell dimensions			
a, *b*, *c* (Å)	83.40, 83.40, 83.40	28.23, 59.12, 45.42	142.71, 142.71, 83.13
α, β, γ (°)	90, 90, 90	90, 106.73, 90	90, 90, 120
Resolution (Å)	24.07–2.60 (2.64–2.60)	43.31–1.60 (1.64–1.60)	32.79–3.17 (3.23–3.17)
R_{sym} or R_{merge}	0.139 (0.655)	0.061 (0.123)	0.192 (0.777)
$I/\sigma I$	46.2 (7.3)	17.1 (13.2)	18.1 (6.2)
Completeness (%)	98.6 (99)	99.9 (99.5)	92.2 (96.0)
Redundancy	37.0 (36.7)	3.7 (3.6)	58.8 (57.6)
Refinement			
Resolution (Å)	24.07–2.60	43.41–1.60	32.79–3.17
Number of reflections	3,328	17,905	8,196
R_{work}/R_{free}	0.185/0.254	0.189/0.229	0.236/0.279
Number of atoms	657	1449	1865
Protein	624	1246	1850
Ligand/ion	N/A	N/A	N/A
Water	33	203	15
B factors			
Protein	42.58	5.158	93.63
Ligand/ion	N/A	N/A	N/A
Water	41.52	18.27	65.53
Rmsds			
Bond lengths (Å)	0.002	0.023	0.003
Bond angles (°)	0.588	2.018	0.689
Ramachandran plot			
Preferred regions (%)	94.3	94.9	88.5
Allowed regions (%)	5.7	4.4	6.6
Outliers (%)	0	0.7	4.9

Data for the highest resolution shell are shown in parentheses. N/A, not applicable.

a second α helix (H2: Pro1284–Arg1295) and finally to a 7 residue unstructured C-terminal segment (Glu1296–His1302). Two hydrophobic cores are present in E4B U box. The first hydrophobic core holds together the central α helix H1 and the region surrounding the central β sheet, whereas the second core involves the C-terminal α helix H2 packing against loop L1 (Figure 1B). The overall fold of E4B is similar to that of other U box domains (Andersen et al., 2004; Ohi et al., 2003; Xu et al., 2006; Zhang et al., 2005).

Crystal Structure of the E4B U Box Domain

To complement the NMR spectroscopy study, we determined the crystal structure of the U box domain of E4B (aa 1208–1302) at a resolution of 2.6 Å (Figure 1C). The crystallography statistics are provided in Table 2. Crystals grew in space group P432, with one molecule of E4B per asymmetric unit, consistent with a monomeric structure. Phasing was done by molecular replacement (MR) using the NMR-derived structure of E4B. Final R factors are R_{work} = 18.5% and R_{free} = 25.4%. The electron density is clear for most of the U box domain, the only disordered parts being the N-terminal residues 1208–1225 and C-terminal residues 1301–1302. These are the same regions of the NMR structure that lacked a defined conformation. The $2F_o - F_c$ σ_A-weighted electron density map for E4B is shown in Figure S1A,available online.

The crystal structure and average NMR structure superimpose well, with an rmsd of 1.04 Å for the backbone atoms N, Cα, and C′ of residues 1228–1299 (Figure 1C). In the crystal lattice, there is no pairing of U box domains corresponding to the previously identified interface in homodimeric U box proteins, a result also consistent with the monomeric nature of E4B U box (Figure S1B).

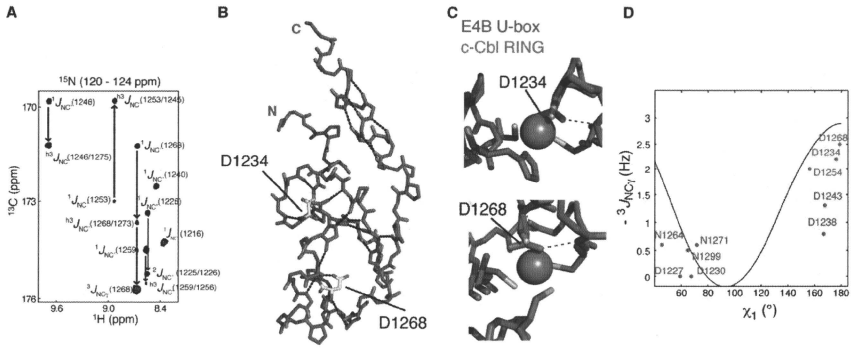

Figure 2. Identification of Hydrogen Bonds in E4B U Box by NMR Spectroscopy

(A) A region from the constant time 3D *J*-HNCO NMR spectrum of E4B U box showing peaks correlated through $^{1}J_{NC'}$, $^{2}J_{NC'}$, $^{3}J_{NC\gamma}$, and $^{h3}J_{NC'}$ scalar couplings.

(B) The 19 H bonds in E4B U box that are listed in Table S1 were identified through $^{h3}J_{NC'}$ scalar coupling measurements. The dotted lines represent these H bonds. Residues Asp1232 and Asp1268 for which side-chain $^{3}J_{NC\gamma}$ scalar couplings were measured are shown. Asp1232 and Asp1268 correspond to the zinc binding regions of RING domains.

(C) Asp1232 and Asp1268 of E4B U box approximately occupy the zinc centers (purple spheres) in c-Cbl RING domain (PDB ID code 1FBV) when the U box and RING domains are superimposed. H bonds involving the two aspartate side chains were determined from $^{3}J_{NC\gamma}$ scalar coupling measurements and are shown by the dashed lines.

(D) Calibration curve for the dihedral-angle (χ_1) dependence of $^{3}J_{NC\gamma}$ scalar couplings in aspartate and asparagine residues. Blue and red points correlate experimental $^{3}J_{NC\gamma}$ and corresponding χ_1 angle values from the crystal structure of E4B U box. The red points correspond to residues for which a side-chain carbonyl participates in an H bond as determined from $^{3}J_{NC\gamma}$ scalar couplings. See also Table S1 for the values of measured coupling constants.

Hydrogen-Bond Network in E4B Determined Experimentally from Scalar Couplings

An extensive hydrogen-bond (H bond) network is predicted from the solution and crystal structures of E4B U box. Canonical H–N···O=C H bonds can be detected experimentally via long-range $^{h3}J_{NC'}$ scalar couplings that connect the ^{15}N nucleus of the donor amino acid to the carbonyl ^{13}C nucleus of the acceptor (Cordier and Grzesiek, 1999). From such measurements in E4B, a total of 19 H bonds were unambiguously identified. Twelve are backbone H bonds that link interstrand residues in the β sheet as well as i and i + 4 residues within the central and C-terminal helices (Figures 2A and 2B; Table S1). Seven H bonds were identified in loop regions (Table S1).

From comparison of the structures of E4B U box and the C3HC4-type zinc binding RING finger motif of c-Cbl (Zheng et al., 2000), E4B residues Asp1234, Met1237, Asp1254, and Ser1256 are found to approximate the histidine and cysteine residues in the first zinc binding site of the RING motif. Similarly, Ser1249, Thr1251, Asp1268, and Asn1271 are the residues corresponding to the second zinc binding site (Figure 2C). Noticeably, the carboxylate groups of Asp1234 and Asp1268 roughly occupy the place of cationic zinc metal centers in the first and second zinc binding sites in the RING motif, respectively. Supporting this observation, the side-chain carbonyls of Asp1234, Asp1254, and Asp1268 were identified through $^{3}J_{NC\gamma}$ scalar couplings to be involved in H bonds (Figures 2B and 2C; Table S1). The dihedral angles χ_1 (defined by atoms N-C_α-C_β-C_γ) measured for Asp1234, Asp1254, and Asp1268 in the crystal structure of E4B U box and the corresponding experimental $^{3}J_{NC\gamma}$ scalar couplings are in good agreement with the predicted dependence of $^{3}J_{NC\gamma}$ on χ_1 values (Juranić et al., 2005) (Figure 2D). This is consistent with the aspartate side chains adopting a defined conformation in solution. Notice that $^{3}J_{NC\gamma}$ scalar couplings for E4B surface Asp1238 and Asp1243 are not predictive of the angles measured in the crystal structure (angle difference ≥ 30°), an indication that these side chains are in a state of free rotation around χ_1 in solution. $^{3}J_{NC\gamma}$ values for other aspartate and asparagine residues of E4B are consistent with the χ_1 dihedral angles measured in the crystal structure (Figure 2D). Taken together, our data show that the U box motif is stabilized by a network of H bonds with some H bonds substituting for Zn^{+2} chelation in RING domains.

Comparison of E4B U Box Monomer to Dimeric U Box Domains

E4B U box is monomeric unlike all other U box domains characterized previously, which have a conserved dimeric topology (Vander Kooi et al., 2006; Xu et al., 2006; Zhang et al., 2005). This difference in oligomerization state can be understood from comparison of the structure and amino acid sequence of E4B U box to those of dimeric U box proteins such as CHIP or Prp19 (Figures 3A and 3B). In mouse CHIP, homodimerization is mediated by the hydrophobic residues Tyr231, Ile246, Ile282, and Ala286 and an asparagine (Asn284) that forms H bonds with the same residue of the complementary CHIP molecule. The corresponding first four residues in human E4B are all charged: Glu1231, Arg1246, Glu1281, and Glu1285, and two are conserved in *S. cerevisiae* Ufd2 (Figure 3A). The hydrophobic nature

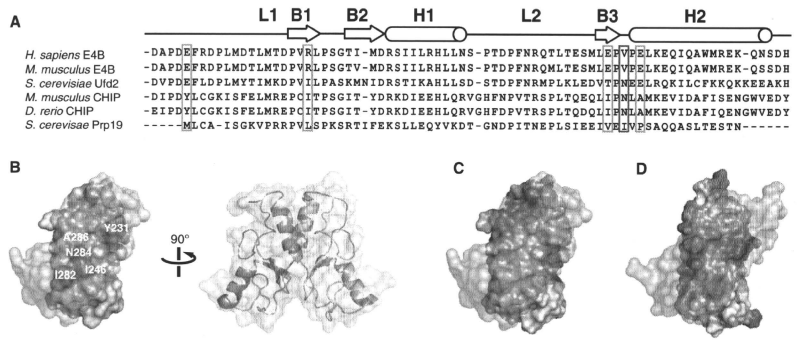

Figure 3. Electrostatic Surface Potentials of E4B and CHIP U Box Domains Affect Oligomerization States

(A) Sequence alignment of U box domains from different E3 ubiquitin ligases indicating locations of secondary-structure elements. CHIP and Prp19 are dimers whereas Ufd2 and E4B are monomers. Key CHIP and Prp19 residues mediating homodimerization are highlighted. Hydrophobic residues in CHIP and Prp19 (green box) correspond to charged residues in E4B, whereas an asparagine residue (Asn284) in mouse CHIP (blue box) is replaced by a valine residue (Val1283) in human E4B.

(B) Molecular representation of mouse CHIP homodimer showing the important dimerization interface residues described in (A).

(C) Electrostatic surface potential of mouse CHIP U box homodimer (PDB ID code 2C2V) showing predominantly nonpolar character at the dimerization interface. The foremost protomer is rendered transparent for clarity.

(D) Electrostatic surface potential of a hypothetical homodimer of E4B U box showing a negatively charged dimer interface.

of the interface in CHIP is in stark contrast with the corresponding negatively charged surface of a hypothetical E4B dimer, likely explaining the monomeric state of human E4B U box (Figures 3C and 3D). This also applies to mouse E4B U box, whose NMR structure was reported recently (Nordquist et al., 2010). Despite the dissimilarities in oligomerization states of E4B and CHIP U boxes, we note that full-length mouse CHIP has an asymmetric conformation in which the E2 binding site of one of the U box domains is blocked (Zhang et al., 2005). Thus, a CHIP dimer, like the E4B monomer, only binds one E2 ubiquitin-conjugating enzyme.

Structure of the Complex of Human E4B U Box and UbcH5c

The ability of the human ubiquitin ligase E4B to participate in its own ubiquitylation and that of bacterial substrates was shown previously (Hatakeyama et al., 2001). In these in vitro assays, E4B was mixed with E1, different E2 enzymes, ubiquitin, and bacterial lysate, and then immunoblotted with antibodies against ubiquitin to detect the ubiquitylation that occurred (Hatakeyama et al., 2001). These experiments showed that ubiquitylation required the U box domain of E4B and that the enzymatic reaction was most efficient with the E2-conjugating enzymes UbcH5c and Ubc4. Little enzymatic activity was detected when other E2s including Ubc2a, Ubc2b, Ubc3, UbcH6, UbcH7, and UbcH8 were present.

Using ITC, we confirmed the interaction of E4B U box and full-length UbcH5c (aa 1–147) and Ubc4 (aa 1–147). A dissociation constant (K_D) of 67.1 ± 5.4 μM at 22°C was determined for the E4B U box–UbcH5c interaction with a stoichiometry close to unity (n = 0.99 ± 0.05) (Figure 4A). The interaction is endothermic with an unfavorable observed enthalpy change (ΔH_{obs} = 2.9 kcal·mol^{-1}) but is entropically favored ($-T\Delta S_{obs}$ = −8.5 kcal·mol^{-1}). Similar thermodynamic parameters were obtained for the calorimetric titration of Ubc4 with E4B U box (data not shown). The control ITC dilution experiment in which E4B U box is injected into a buffer solution does not show any marked change in heat of dilution as the concentration of E4B U box increases in the calorimeter cell, consistent with a monomeric state of E4B U box (Figure 4A).

To gain additional insight into these interactions, we attempted crystallization of E4B U box in complex with Ubc4 and UbcH5c. From these trials, we initially obtained crystals of Ubc4 (aa 1–147) alone and determined its structure to a resolution of 1.6 Å by MR using the atomic coordinates of UbcH5c (Protein Data Bank [PDB] ID code 1X23) (Figure S2A). The final R factors are R_{work} = 18.9% and R_{free} = 22.9%. Refinement statistics are summarized in Table 2. The crystals have a space group of $P2_1$ and contain one molecule of Ubc4 in the asymmetric unit. The electron density is well defined, as illustrated by the $2F_o - F_c$ σ_A-weighted map shown in Figure S2B.

We were able to determine the crystal structure of UbcH5c (aa 1–147) in complex with the U box domain of human E4B (aa 1208–1302) to a resolution of 3.17 Å (Figure 4B). The crystals have one molecule each of UbcH5c and E4B U box per asymmetric unit in the space group P622. Phasing was done by MR using the crystal structures of free human Ubc4 and E4B U box, both from this study, as starting models. The final R factors are R_{work} = 23.6% and R_{free} = 27.9%, and refinement statistics can be found in Table 2. The resulting electron density map has a good fit for most regions of E4B and UbcH5c, except for the first 18 N-terminal residues (aa 1208–1225) and last two

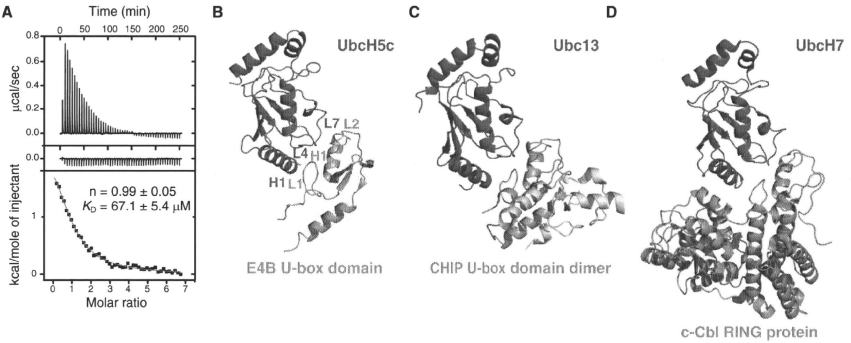

Figure 4. Interaction of E4B U Box with UbcH5c and Ubc4 E2-Conjugating Enzymes

(A) Isothermal titration calorimetry of UbcH5c with E4B U box. Shown are the integrated heat measurements from injecting 3 mM E4B U box into the calorimeter cell containing UbcH5c at an initial concentration of 100 µM (top panel) or buffer solution (middle panel). A standard one-site model was used for curve fitting (bottom panel) in the determination of K_D and stoichiometry (n), the values of which are shown.

(B) Crystal structure of human E4B U box in complex with UbcH5c.

(C) Crystal structure of mouse CHIP U box in complex with Ubc13 (PDB ID code 2C2V).

(D) Crystal structure of the human c-Cbl RING E3 ligase in complex with UbcH7 (PDB ID code 1FBV). See also Figure S2.

C-terminal residues (1301 and 1302) of E4B, which are not visible in the electron density. These regions of the protein also lack a stable conformation in the solution and crystal structures of E4B (vide supra). Ten surface residues of UbcH5c and nine of E4B with long side chains—arginine, lysine, or methionine—are poorly defined with incomplete electron density. In the protein cores and at the interface of the two proteins in the crystal, all residues have electron density guiding their position. A $2F_o - F_c$ σ_A-weighted electron density map is shown in Figure S3. Noticeably, of the three crystals used to elucidate the E4B U box–UbcH5c structure, all had a missing layer of electron density equal to one-third of the unit cell. This is likely due either to one-dimensional twinning or another crystalline disorder(s). The lack of electron density could originate from the N- and C-terminal flexible segments of E4B, which point toward the disordered region of the crystals. No crystals of the complex could be obtained with shorter versions of E4B. Further remarks on this subject are presented in Supplemental Discussion.

In the crystal, the most energetically favorable interface between E4B U box and UbcH5c, as determined using PISA (Krissinel and Herrick, 2007), occurs along each of the crystallographic six-fold symmetry axes. As explained below, this also corresponds to the binding site identified in solution using NMR spectroscopy. The relative positioning of the two proteins is such that H1, L4, and L7 of UbcH5c make contacts with L1, H1, and L2 of E4B, respectively (Figure 4B). Polar interactions at the interface include a salt bridge between E4B U box Asp1238 and UbcH5c Lys8 (Figure 5A). Based on (N)H···O(C) distances shorter than 3.8 Å, there likely are intermolecular H bonds involving the following atoms: E4B-Leu1236 O and UbcH5c-Arg5 NH1, E4B-Pro1269 O and UbcH5c-Ser94 OG, E4B-Asn1264 ND2 and UbcH5c-Phe62 O, E4B-Asn1264 O and UbcH5c-Lys63 NZ, and E4B-Arg1272 and Gln92 OG1 (Figure 5A). There are three hydrophobic clusters at the interface. The first, composed of Leu1236, Met1237, Ile1257, Arg1260, His1261, and Asn1264 of E4B, forms a deep pocket where Phe62 of UbcH5c is completely buried (Figure 5B). With Arg1260 close to Phe62 at 4.5 Å, there is a possible cation–π interaction between the guanidinium group and the phenyl ring. A similar cation–π interaction is present in mouse and zebrafish CHIP U box complexes (Xu et al., 2008; Zhang et al., 2005). The second cluster, composed of Leu1236, Met1253, His1261, Pro1269, and Phe1270 of E4B, forms a channel in which Ser94, Pro95, and Ala96 of UbcH5c are located (Figure 5B). This UbcH5c motif, termed S-P-A, is conserved and is part of a similar interface in the E2-E3 structures of mouse and zebrafish CHIP in complex with Ubc13 and UbcH5a, respectively (Xu et al., 2008; Zhang et al., 2005), and in the RING domain protein TRAF2 bound to Ubc13 (Yin et al., 2009). The final hydrophobic cluster encompasses E4B Leu1236 and Met1237, which both contact the surface of UbcH5c made up of Ala2, Leu3, Lys4, Arg5, and Lys8 (Figure 5C). Overall, the E4B–UbcH5c interface resembles those of other E2-E3 complexes such as CHIP-Ubc13-Uev1a (Zhang et al., 2005) and c-Cbl-UbcH7 (Zheng et al., 2000) where the E3 is a U box- or RING domain-containing protein (Figures 4C and 4D).

Mapping the E4B Interaction Interface with UbcH5c and Ubc4 in Solution

To further probe how E4B U box binds UbcH5c and Ubc4 in solution and validate the crystal structure of E4B U box–UbcH5c complex, we acquired a series of ^{1}H-^{15}N HSQC NMR spectra on ^{15}N-labeled E4B U box, alone and titrated with nonlabeled Ubc4 (aa 1–147) or UbcH5c (aa 1–147) (Figures 6A and 6B).

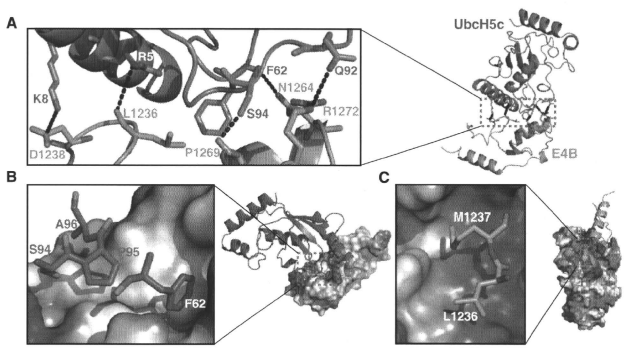

Figure 5. Interaction Interface between E4B U Box and UbcH5c
(A) E4B U box and UbcH5c interface showing possible salt bridges and hydrogen bonds.
(B) E4B U box and UbcH5c interface showing how F62 and S94-P95-A96 (S-P-A motif) of UbcH5c interact with E4B U box.
(C) E4B U box and UbcH5c interface illustrating how L1236 and M1237 of E4B U box interact with UbcH5c. See also Figure S3 for the electron density map of E4B U box–UbcH5c complex.

Only one set of E4B signals was observed during the entire titration with either UbcH5c or Ubc4. A subset of these signals shifted and broadened, indicating that the exchange between E4B in the free state and bound to Ubc4 or UbcH5c is fast to intermediate on the NMR chemical shift timescale. This exchange regime is consistent with the K_D of 67.1 ± 5.4 μM for the E4B U box–UbcH5c interaction derived from ITC measurements (Figure 4A). The E4B residues for which changes occurred in the ^{1}H-^{15}N HSQC spectrum during titration by Ubc4 or UbcH5c were mapped on the structure of E4B. As shown in Figure 6C, these residues are all in the vicinity of the most favorable binding interface identified in the crystal structure of E4B U box–UbcH5c complex.

To identify the binding site of the E2-conjugating enzymes, complementary NMR experiments were performed where ^{15}N-labeled Ubc4 and UbcH5c were titrated with nonlabeled E4B U box (Figures 6D and 6E). For these studies, we used the previously published resonance assignments of human Ubc4 (Farrow et al., 2000). Because of the 97% amino acid sequence identity between Ubc4 and UbcH5c and their similar structures, these assignments could also be used for UbcH5c (Jensen et al., 1995). As expected, the chemical shift changes observed for the two E2 enzymes were similar (Figures 6D and 6E). Residues exhibiting chemical shift perturbations were highlighted in the crystal structure of E4B U box–UbcH5c. Perturbed resonances primarily come from residues in loops L4 and L7 and the N-terminal helix H1 of UbcH5c, and fit well the binding interface seen in the crystal structure of E4B U box–UbcH5c complex (Figure 6F). This demonstrates a close agreement between the binding interface in solution and in the crystalline state.

Interestingly, six residues conserved in Ubc4 and UbcH5c that are distant from the binding interface also experience shifts in their NMR signals upon interaction with E4B U box (Figure 6G). As discussed next in light of previous work on the interaction of UbcH5b and the RING domain of E3 ubiquitin ligase CNOT4 (Dominguez et al., 2004; Ozkan et al., 2005), the observed changes in chemical shifts suggest that E4B U box could regulate UbcH5c and Ubc4 through an allosteric mechanism.

DISCUSSION

The question of whether U box and related RING E3 ubiquitin ligases are only adaptor proteins that bring substrate and E2 in close proximity or contribute also to an induced activating conformational change in their cognate E2 enzymes has been subject to debate (Deshaies and Joazeiro, 2009). The crystal structure of human E4B U box–UbcH5c complex does not reveal any change in conformation when compared to the structures of the two proteins in their unbound state. NMR spectroscopy is a very sensitive technique to probe changes in conformations. As mentioned above, upon complex formation, shifts in ^{1}H and ^{15}N signals of surface residues of E4B U box and UbcH5c map to the binding interface identified in the crystal structure, therefore validating this interface in solution. Importantly, after addition of E4B U box, we also observed changes in chemical shifts for six resonances associated with amino acids in UbcH5c and Ubc4 that are distant from the interface: Thr36, Ile37, Asp87, Ser91, Gln92, and Ile106 (Figures 6D–6G). This is consistent with subtle changes in flexibility or conformation, or both, that propagate away from the E4B binding site. From their location in UbcH5c and Ubc4, these residues may connect the binding interface to the active site cysteine (Cys85) (Figure 6G), suggesting a possible allosteric regulation of the enzymatic activity by E4B through alteration of the E2 active site.

It was previously shown that binding of the RING domain of human E3 ubiquitin ligase CNOT4 to the E2 enzyme UbcH5b allosterically enhances the release of ubiquitin from UbcH5b-ubiquitin thioester (Ozkan et al., 2005). Because UbcH5b is

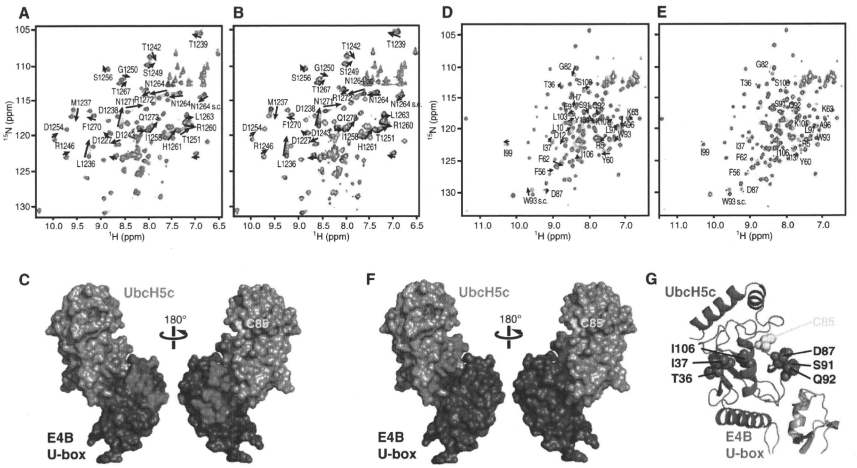

Figure 6. NMR Titrations and Mapping of Interaction Interfaces in E4B U Box, UbcH5c, and Ubc4

(A and B) Superposition of the ^{1}H-^{15}N HSQC titration spectra of ^{15}N-labeled E4B U box from free (black) to the bound (red) states with nonlabeled Ubc4 (A) and UbcH5c (B). The arrows indicate the directions of the titrations.

(C) In the crystal structure of E4B U box and UbcH5c complex, E4B residues affected by UbcH5c titration are colored red (signals with chemical shift changes ≥ 0.02 ppm) or blue (weakened or disappeared signals, namely those of Asp1234, Leu1236, Asp1238, Leu1247, Ile1258, Asn1271, and Arg1272). The active site Cys85 is shown in yellow.

(D and E) Superposition of the ^{1}H-^{15}N HSQC titration spectra of ^{15}N-labeled Ubc4 (D) or UbcH5c (E) from the free (black) to the bound (red) states with nonlabeled E4B U box. The arrows indicate the directions of the titrations.

(F) In the crystal structure of E4B U box and UbcH5c complex, UbcH5c residues affected by E4B U box titration are colored red (signals with chemical shift changes from 0.03 to 0.06 ppm) or blue (chemical shift changes from 0.07 to 0.16 ppm). The active site Cys85 is shown in yellow.

(G) UbcH5c residues distant from the binding interface with E4B U box and for which changes in chemical shifts were detected are shown in gray. The active site Cys85 is shown in yellow.

highly similar to UbcH5c and Ubc4 (97.3% and 99.3% amino acid identity, respectively) and the U box and RING domains bind the same surface of the E2 enzyme, it is likely that E4B U box contributes to the activation of UbcH5c and Ubc4. Supporting this possibility, the UbcH5c and Ubc4 residues not involved in E3 binding and for which changes in chemical shifts were observed upon interaction with the U box domain are the same or in the vicinity of residues in UbcH5b (Ile37, Ile88, Leu89, Ile106, and Asn114), which when mutated inhibited the RING domain-stimulated release of ubiquitin from the active site cysteine (Ozkan et al., 2005). More work will be needed to test this allosteric activation hypothesis and to understand how ubiquitin released from E2 is transferred to the substrate.

To examine how E4B U box bound to UbcH5c is positioned in the context of full-length E4B, we generated a model by superimposing the structure of human E4B U box–UbcH5c complex onto the structures of budding yeast Ufd2 (Tu et al., 2007) and human UbcH5c bound noncovalently to ubiquitin (Brzovic et al., 2006) (Figure 7). When its first 187 N-terminal amino acids are excluded, Ufd2 has high sequence similarity (i.e., 56% similarity and 30% identity) with the C-terminal half of human E4B (aa 560–1302), therefore making Ufd2 (aa 188–961) a reasonable template for this segment of E4B. The region of similarity encompasses a large N-terminal core domain made of five repeating units that resemble tandem Armadillo repeats and also includes the C-terminal U box domain (Figure 7).

When the U box in the E4B U box–UbcH5c complex is overlaid to the U box of Ufd2, the positioning of UbcH5c has few steric or surface charge clashes with the core region of Ufd2. Moreover, the small clashes are likely insignificant because structures of Ufd2 from two crystal forms revealed flexibility in the hinge region connecting the U box to the rest of the protein (Tu et al., 2007). Normal mode calculations performed with NOMAD (Lindahl et al., 2006) on Ufd2 also support a hinge-bending motion of the U box relative to the protein core (data not shown). In the overlaid structures, the orientation of UbcH5c is such that its noncovalent ubiquitin binding site can be occupied by ubiquitin. Also unhindered is the active site cysteine of UbcH5c to which a ubiquitin molecule can be covalently linked without creating any steric clash with the rest of the complex.

Presumably, the large E4B domain made of tandem Armadillo repeats or residues N-terminal from this domain and lacking in

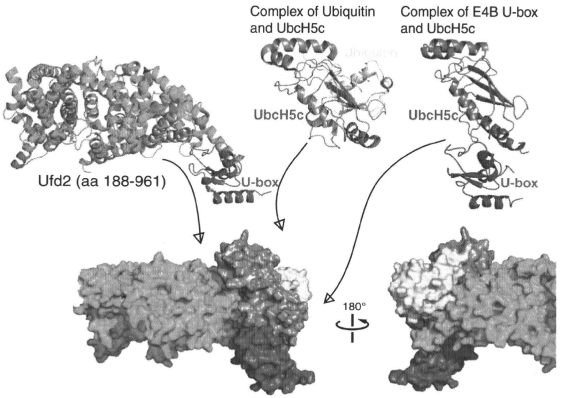

Figure 7. Model Structure of E4B, UbcH5c, and Ubiquitin Ternary Complex
The structures of budding yeast Ufd2 (aa 188–961 from PDB ID code 2QIZ), human UbcH5c-ubiquitin (PDB ID code 2FUH), and human E4B U box–UbcH5c (this study) were superimposed to model the complex. Ubiquitin (yellow), UbcH5c (gray), and Ufd2 (body in green and U box in blue) fit together in the model with very few steric clashes and leave the active site cysteine of UbcH5c (red) accessible to react with a ubiquitin molecule.

our model, or both, are involved in the recognition of substrate proteins. Work is in progress to characterize full-length E4B and its interaction with a protein substrate, a requirement to understand the ubiquitin transfer mechanism.

EXPERIMENTAL PROCEDURES

Protein Preparation

The cDNAs of full-length Ubc4 and UbcH5c were cloned in a pT7.7 vector encoding an N-terminal noncleavable His_6 tag, whereas a DNA segment corresponding to aa 1203–1302 of E4B was inserted in a pET28b vector encoding an N-terminal His_6 tag preceding a thrombin cleavage site. The proteins were produced in *Escherichia coli* BL21(DE3) cells (Novagen) grown in LB media at 37°C until an A_{600} of about 0.8, transferred to 15°C, and then induced with 1 mM final concentration of IPTG 45 min later. Cells were harvested 12–16 hr afterward.

Cell pellets were resuspended in 50 mM sodium phosphate (pH 7.5), 300 mM NaCl (buffer 1) supplemented with 5 mM imidazole and lysed using a high-pressure homogenizer (Emulsiflex C-5; Avestin). The soluble and insoluble fractions were separated by centrifugation and the lysate was loaded onto an Ni^{2+}-NTA column (QIAGEN). Buffer 1 with 20 and 500 mM imidazole was used to wash the column and elute the protein, respectively. Where applicable, the His_6 tag was then cleaved with thrombin at room temperature overnight, leaving the sequence GSHKF at the N terminus of E4B U box. All proteins were passed through a Superdex 75 size-exclusion chromatography column (GE Healthcare) equilibrated with buffer 1.

Isotopically labeled proteins were produced using similar methods but replacing LB media with M9 media containing 1 g/l $[^{15}N]NH_4Cl$, 4 g/l unlabeled glucose or 2 g/l ^{13}C-enriched glucose, 1 g/l Isogro, or 10% (v/v) Silantes OD2 media that are ^{15}N or $^{15}N/^{13}C$ enriched and H_2O or D_2O (Botuyan et al., 2004). Isotopes were purchased from Isotec and CIL.

NMR Spectroscopy

All NMR spectra were recorded at 25°C using Bruker Avance spectrometers operating at proton frequencies of 500 and 600 MHz (with cryoprobe). Multiple samples of nonlabeled, ^{15}N-labeled, $^{15}N/^{13}C$-labeled, and $^{15}N/^{13}C/^{2}H$-labeled E4B U box were prepared at concentrations of 0.5–2 mM in 20 mM sodium phosphate buffer (pH 7.0), 50 mM NaCl. Backbone and side-chain resonance assignments were carried out using standard NMR experiments including HNCO, HNCACO, HNCA, HNCOCA, HNCACB, HNCOCACB, CCONH-TOCSY, HCCONH-TOCSY, HBHACONH, HCCH-TOCSY, ^{1}H-^{15}N TOCSY-HSQC, and 2D TOCSY (Ferentz and Wagner, 2000). Interproton distance restraints were derived from ^{15}N-edited NOESY (mixing time of 100 ms) and ^{13}C-edited NOESY (mixing time of 100 ms) spectra of ^{15}N- and $^{15}N/^{13}C$-labeled E4B, respectively, as well as from a series of 2D NOESY spectra of nonlabeled E4B U box recorded with mixing times of 20, 30, 50, 60, and 100 ms. All data were processed with NMRPipe/NMRDraw (Delaglio et al., 1995) and analyzed with NMRView (Johnson and Blevins, 1994). Assignment of nuclear Overhauser effect (NOE) signals was facilitated by using the noeassign module of CYANA 2.1 (Güntert, 2004).

Identification of Hydrogen Bonds in E4B U Box

The H bond $^{h3}J_{NC'}$, peptide bond $^{1}J_{NC'}$, and intraresidue $^{3}J_{NC'}$ scalar coupling constants were measured using constant time 3D *J*-HNCO experiments (Cordier et al., 1999a, 1999b; Cornilescu et al., 1999). The *J*-HNCO spectra were recorded with constant times of 35 and 70 ms and with evolution times of 16, 20, 24, 28, 32, 33, and 34 ms and 40, 50, 54, 65, 66, and 66.5 ms. The coupling constants were determined by fitting the time evolution of all observed NC′ couplings. H bond d_{HO} distances [(N)H···O(C)] and H-bond acceptor angles [(N)H···O=C] listed in Table S1 were estimated from the magnitudes of the couplings (Juranić and Macura, 2001; Juranić et al., 2006).

NMR Structure Calculations

NMR structure calculations were performed with CYANA 2.1 (Güntert, 2004) using a total of 1368 NOE-derived interproton distances, 36 H bond distances identified from slow-exchanging amide protons and from measurement of scalar couplings as explained above, and 46 dihedral ϕ and ψ angle restraints derived from TALOS analysis (Cornilescu et al., 1999). The structures were then refined by simulated annealing with Xplor (Schwieters et al., 2003). For further validation of the structures, 63 ^{1}H-^{15}N residual dipolar coupling (RDC) restraints were included in a separate set of calculations using Xplor. The RDCs were measured by weak alignment of E4B U box in stretched polyacrylamide gel (Chou et al., 2001).

Isothermal Titration Calorimetry

All ITC measurements were recorded at 22°C with a VP-ITC titration calorimeter (MicroCal). All protein samples were in 50 mM Tris-HCl (pH 7.5), 20 mM NaCl at concentrations of 100 μM for UbcH5c and Ubc4 and 3 mM for E4B U box. The calorimeter syringe was used to deliver E4B U box as 50 injections (1 × 3 μl followed by 49 × 6 μl) at 5 min intervals into the calorimetric cell containing 1.42 ml of UbcH5c or Ubc4 solution. Control experiments were performed under identical conditions to determine the heat signals that arise from injecting E4B U box into the buffer solution. The initial data point (from the first 3 μl injection) was routinely deleted. Data were analyzed by Levenberg-Marquardt nonlinear regression fitting of each ITC isotherm using a model corresponding to one independent binding event (Turnbull and Daranas, 2003).

Crystallization and X-Ray Structure Determination

All crystals were obtained at 22°C using the hanging-drop vapor-diffusion method by mixing 1 μl of 1 mM protein solution and 1 μl of precipitant solution. The proteins were in 50 mM Tris-HCl (pH 7.5), 50 mM NaCl. Crystals of free E4B U box and E4B U box–UbcH5c complex grew overnight in 2 M tacsimate and 4 M sodium formate, respectively, whereas crystals of Ubc4 formed in 2–4 days in 2.0 M sodium formate, 0.1 M sodium acetate trihydrate (pH 4.6). The crystals were cryoprotected by soaking in the respective mother liquor supplemented with 30% glucose and then flash-frozen in liquid nitrogen.

Diffraction data were collected at the Advanced Photon Source 19-BM beamline, Argonne National Laboratory, for E4B U box and E4B U box–UbcH5c complex (wavelength was 0.97918 Å) and using a Rigaku/MSC CuKα Microfocus 007 diffractometer at a wavelength of 1.54 Å for Ubc4. Data were integrated, scaled, and merged using HKL2000 (Otwinowski and Minor, 1997). For all structures, phasing by molecular replacement was done using Phaser (McCoy et al., 2007). Initial model building was performed using Coot (Emsley and Cowtan, 2004). Refinement of the structures of E4B U box in the free state and E4B U box–UbcH5c complex was done using PHENIX (Adams et al., 2002), whereas refinement of the structure of Ubc4 was carried out using REFMAC5 (Murshudov et al., 1997).

ACCESSION NUMBERS

Atomic coordinates and structure factors for the crystal structures of E4B U box, E4B U box–UbcH5c complex, and Ubc4 and the NMR structure of E4B U box have been deposited in the Protein Data Bank under ID codes 1L1X, 3L1Z, 3L1Y, and 2KRE, respectively.

SUPPLEMENTAL INFORMATION

Supplemental Information includes Supplemental Discussion, three figures, and one table and can be found with this article online at doi:10.1016/j.str.2010.04.017.

ACKNOWLEDGMENTS

We acknowledge the use of beamline 19-BM at Argonne National Laboratory, Structural Biology Center at the Advanced Photon Source (APS). Argonne is operated by UChicago Argonne, LLC, for the U.S. Department of Energy, Office of Biological and Environmental Research under contract DE-AC02-06CH11357. We thank Younchang Kim at APS for assistance with X-ray data collection. We thank Ema Stokasimov for her early contribution to this project. Partial support from National Institutes of Health grant CA109449 and a March of Dimes Basil O'Connor scholarship to G.M. is gratefully acknowledged. J.R.T. acknowledges support from the Minnesota Partnership for Biotechnology and Medical Genomics. Y.N. was a recipient of a Kendall-Mayo postdoctoral fellowship in biochemistry.

Received: December 16, 2009
Revised: March 26, 2010
Accepted: April 21, 2010
Published: August 10, 2010

REFERENCES

Adams, P.D., Grosse-Kunstleve, R.W., Hung, L.-W., Ioerger, T.R., McCoy, A.J., Moriarty, N.W., Read, R.J., Sacchettini, J.C., Sauter, N.K., and Terwilliger, T.C. (2002). PHENIX: building new software for automated crystallographic structure determination. Acta Crystallogr. D Biol. Crystallogr. *58*, 1948–1954.

Andersen, P., Kragelund, B.B., Olsen, A.N., Larsen, F.H., Chua, N.H., Poulsen, F.M., and Skriver, K. (2004). Structure and biochemical function of a prototypical *Arabidopsis* U-box domain. J. Biol. Chem. *279*, 40053–40061.

Aravind, L., and Koonin, E.V. (2000). The U box is a modified RING finger—a common domain in ubiquitination. Curr. Biol. *10*, R132–R134.

Botuyan, M.V., Nominé, Y., Yu, X., Juranić, N., Macura, S., Chen, J., and Mer, G. (2004). Structural basis of BACH1 phosphopeptide recognition by BRCA1 tandem BRCT domains. Structure *12*, 1137–1146.

Brzovic, P.S., Lissounov, A., Christensen, D.E., Hoyt, D.W., and Klevit, R.E. (2006). A UbcH5/ubiquitin noncovalent complex is required for processive BRCA1-directed ubiquitination. Mol. Cell *21*, 873–880.

Chou, J.J., Gaemers, S., Howder, B., Louis, J.M., and Bax, A. (2001). A simple apparatus for generating stretched polyacrylamide gels, yielding uniform alignment of proteins and detergent micelles. J. Biomol. NMR *21*, 377–382.

Cordier, F., and Grzesiek, S. (1999). Direct observation of hydrogen bonds in proteins by interresidue $^{3h}J_{NC'}$ scalar couplings. J. Am. Chem. Soc. *121*, 1601–1602.

Cordier, F., Dingley, A.J., and Grzesiek, S. (1999a). A doublet-separated sensitivity-enhanced HSQC for the determination of scalar and dipolar one-bond J-couplings. J. Biomol. NMR *13*, 175–180.

Cordier, F., Rogowski, M., Grzesiek, S., and Bax, A. (1999b). Observation of through-hydrogen-bond $^{2h}J_{HC'}$ in a perdeuterated protein. J. Magn. Reson. *140*, 510–512.

Cornilescu, G., Delaglio, F., and Bax, A. (1999). Protein backbone angle restraints from searching a database for chemical shift and sequence homology. J. Biomol. NMR *13*, 289–302.

Delaglio, F., Grzesiek, S., Vuister, G.W., Zhu, G., Pfeifer, J., and Bax, A. (1995). NMRPipe: a multidimensional spectral processing system based on UNIX pipes. J. Biomol. NMR *6*, 277–293.

Deshaies, R.J., and Joazeiro, A.P. (2009). RING domain E3 ubiquitin ligases. Annu. Rev. Biochem. *78*, 399–434.

Dominguez, C., Bonvin, A.M., Winkler, G.S., van Schaik, F.M., Timmers, H.T., and Boelens, R. (2004). Structural model of the UbcH5b/CNOT4 complex revealed by combining NMR, mutagenesis, and docking approaches. Structure *12*, 633–644.

Emsley, P., and Cowtan, K. (2004). Coot: model-building tools for molecular graphics. Acta Crystallogr. D Biol. Crystallogr. *60*, 2126–2132.

Farrow, N.A., Archer, S.J., Wu, Z.J., Camac, D.M., Parsons, T., Rolfe, M., and Domaille, P.J. (2000). Backbone resonance assignment of human UBC4. J. Biomol. NMR *18*, 363–364.

Ferentz, A.E., and Wagner, G. (2000). NMR spectroscopy: a multifaceted approach to macromolecular structure. Q. Rev. Biophys. *33*, 29–65.

Güntert, P. (2004). Automated NMR structure calculation with CYANA. Methods Mol. Biol. *278*, 353–378.

Hatakeyama, S., Yada, M., Matsumoto, M., Ishida, N., and Nakayama, K.I. (2001). U box proteins as a new family of ubiquitin-protein ligases. J. Biol. Chem. *276*, 33111–33120.

Hatakeyama, S., Matsumoto, M., Yada, M., and Nakayama, K.I. (2004). Interaction of U-box-type ubiquitin-protein ligases (E3s) with molecular chaperones. Genes Cells *9*, 533–548.

Huang, L., Kinnucan, E., Wang, G., Beaudenon, S., Howley, P.M., Huibregtse, J.M., and Pavletich, N.P. (1999). Structure of an E6AP-UbcH7 complex: insights into ubiquitination by the E2-E3 enzyme cascade. Science *286*, 1321–1326.

Jensen, J.P., Bates, P.W., Yang, M., Vierstra, R.D., and Weissman, A.M. (1995). Identification of a family of closely related human ubiquitin conjugating enzymes. J. Biol. Chem. *270*, 30408–30414.

Johnson, B.A., and Blevins, R.A. (1994). NMRView: a computer program for the visualization and analysis of NMR data. J. Biomol. NMR *4*, 603–614.

Juranić, N., and Macura, S. (2001). Correlations among $^{1}J_{NC'}$ and $^{h3}J_{NC'}$ coupling constants in the hydrogen-bonding network of human ubiquitin. J. Am. Chem. Soc. *123*, 4099–4100.

Juranić, N., Atanasova, E., Moncrieffe, M.C., Prendergast, F.G., and Macura, S. (2005). Calcium-binding proteins afford calibration of dihedral-angle dependence of $^{3}J_{NC_\gamma}$ coupling constant in aspartate and asparagine residues. J. Magn. Reson. *175*, 222–225.

Juranić, N., Moncrieffe, M.C., Atanasova, E., Macura, S., and Prendergast, F.G. (2006). NMR $^{h3}J_{NC'}$ couplings provide comprehensive geometrical constraints for protein H-bonds in solution. Croat. Chem. Acta *79*, 503–507.

Koegl, M., Hoppe, T., Schlenker, S., Ulrich, H.D., Mayer, T.U., and Jentsch, S. (1999). A novel ubiquitination factor, E4, is involved in multiubiquitin chain assembly. Cell *96*, 635–644.

Koradi, R., Billeter, M., and Wüthrich, K. (1996). MOLMOL: a program for display and analysis of macromolecular structures. J. Mol. Graph. *14*, 51–55, 29–32.

Krissinel, E., and Herrick, K. (2007). Inference of macromolecular assemblies from crystalline state. J. Mol. Biol. *372*, 774–797.

Kuhlbrodt, K., Mouysset, J., and Hoppe, T. (2005). Orchestra for assembly and fate of polyubiquitin chains. Essays Biochem. *41*, 1–14.

Lindahl, E., Azuara, C., Koehl, P., and Delarue, M. (2006). NOMAD-Ref: visualization, deformation and refinement of macromolecular structures based on all-atom normal mode analysis. Nucleic Acids Res. *34*, W52–W56.

Matsumoto, M., Yada, M., Hatakeyama, S., Ishimoto, H., Tanimura, T., Tsuji, S., Kakizuka, A., Kitagawa, M., and Nakayama, K.I. (2004). Molecular clearance of ataxin-3 is regulated by a mammalian E4. EMBO J. *23*, 659–669.

McCoy, A.J., Grosse-Kunstleve, R.W., Adams, P.D., Winn, M.D., Storoni, L.C., and Read, R.J. (2007). Phaser crystallographic software. J. Appl. Crystallogr. *40*, 658–674.

Murshudov, G.N., Vagin, A.A., and Dodson, E.J. (1997). Refinement of macromolecular structures by the maximum-likelihood method. Acta Crystallogr. D Biol. Crystallogr. *53*, 240–255.

Nordquist, K.A., Dimitrova, Y.N., Brzovic, P.S., Ridenour, W.B., Munro, K.A., Soss, S.E., Caprioli, R.M., Klevit, R.E., and Chazin, W.J. (2010). Structural and functional characterization of the monomeric U-box domain from E4B. Biochemistry *49*, 347–355.

Ohi, M.D., Vander Kooi, C.W., Rosenberg, J.A., Chazin, W.J., and Gould, K.L. (2003). Structural insights into the U-box, a domain associated with multiubiquitination. Nat. Struct. Biol. *10*, 250–255.

Otwinowski, Z., and Minor, W. (1997). Processing of X-ray diffraction data collected in oscillation mode. Methods Enzymol. *276*, 307–326.

Ozkan, E., Yu, H., and Deisenhofer, J. (2005). Mechanistic insight into the allosteric activation of a ubiquitin-conjugating enzyme by RING-type ubiquitin ligases. Proc. Natl. Acad. Sci. USA *102*, 18890–18895.

Passmore, L.A., and Barford, D. (2004). Getting into position: the catalytic mechanisms of protein ubiquitylation. Biochem. J. *379*, 513–525.

Pickart, C.M. (2001). Mechanisms underlying ubiquitination. Annu. Rev. Biochem. *70*, 503–533.

Pickart, C.M., and Eddins, M.J. (2004). Ubiquitin: structures, functions, mechanisms. Biochim. Biophys. Acta *1695*, 55–72.

Richly, H., Rape, M., Braun, S., Rumpf, S., Hoege, C., and Jentsch, S. (2005). A series of ubiquitin binding factors connects CDC48/p97 to substrate multiubiquitylation and proteasomal targeting. Cell *120*, 73–84.

Schwieters, C.D., Kuszewski, J.J., Tjandra, N., and Marius Clore, G. (2003). The Xplor-NIH NMR molecular structure determination package. J. Magn. Reson. *160*, 65–73.

Tu, D., Li, W., Ye, Y., and Brunger, A.T. (2007). Structure and function of the yeast U-box-containing ubiquitin ligase Ufd2p. Proc. Natl. Acad. Sci. USA *104*, 15599–15606.

Turnbull, W.B., and Daranas, A.H. (2003). On the value of c: can low affinity systems be studied by isothermal titration calorimetry? J. Am. Chem. Soc. *125*, 14859–14866.

Vander Kooi, C.W., Ohi, M.D., Rosenberg, J.A., Oldham, M.L., Newcomer, M.E., Gould, K.L., and Chazin, W.J. (2006). The Prp19 U-box crystal structure suggests a common dimeric architecture for a class of oligomeric E3 ubiquitin ligases. Biochemistry *45*, 121–130.

Weissman, A.M. (2001). Themes and variations on ubiquitylation. Nat. Rev. Mol. Cell Biol. *2*, 169–178.

Xu, Z., Devlin, K.I., Ford, M.G., Nix, J.C., Qin, J., and Misra, S. (2006). Structure and interactions of the helical and U-box domains of CHIP, the C terminus of HSP70 interacting protein. Biochemistry *45*, 4749–4759.

Xu, Z., Kohli, E., Devlin, K.I., Bold, M., Nix, J.C., and Misra, S. (2008). Interactions between the quality control ubiquitin ligase CHIP and ubiquitin conjugating enzymes. BMC Struct. Biol. *8*, 26.

Ye, Y., and Rape, M. (2009). Building ubiquitin chains: E2 enzymes at work. Nat. Rev. Mol. Cell Biol. *10*, 755–764.

Yin, Q., Lin, S.C., Lamothe, B., Lu, M., Lo, Y.C., Hura, G., Zheng, L., Rich, R.L., Campos, A.D., Myszka, D.G., et al. (2009). E2 interaction and dimerization in the crystal structure of TRAF6. Nat. Struct. Mol. Biol. *16*, 658–666.

Zhang, M., Windheim, M., Roe, S.M., Peggie, M., Cohen, P., Prodromou, C., and Pearl, L.H. (2005). Chaperoned ubiquitylation—crystal structures of the CHIP U box E3 ubiquitin ligase and a CHIP-Ubc13-Uev1a complex. Mol. Cell *20*, 525–538.

Zheng, N., Wang, P., Jeffrey, P.D., and Pavletich, N.P. (2000). Structure of a c-Cbl-UbcH7 complex: RING domain function in ubiquitin-protein ligases. Cell *102*, 533–539.

Cite as: Cold Spring Harb Protoc; 2010; doi:10.1101/pdb.prot5512

Protocol

In Vitro Histone Demethylase Assay

Yu-ichi Tsukada[1,2,3] and Keiichi I. Nakayama[1,2,4]

[1] Division of Cell Biology, Medical Institute of Bioregulation, Kyushu University, Fukuoka 812-8582, Japan
[2] Core Research of Evolutional Science and Technology, Japan Science and Technology Agency, Kawaguchi, Saitama 332-0012, Japan
[3] Precursory Research for Embryonic Science and Technology, Japan Science and Technology Agency, Kawaguchi, Saitama 332-0012, Japan

[4]Corresponding author (nakayaki@bioreg.kyushu-u.ac.jp).

INTRODUCTION

Post-translational modifications of histones play an important role in regulating chromatin dynamics and function. One of the modifications, methylation, occurs on both lysine and arginine residues, and methylation status defines the epigenetic program of a cell by determining chromatin structure and thereby regulating DNA-dependent processes such as transcription. Until recently, histone methylation was considered to be irreversible. However, the discovery of histone demethylases revealed that histone methylation is more dynamic than previously recognized. This protocol describes two different in vitro histone demethylase enzyme reactions and three different methods for measuring histone demethylase activity. The first reaction (type I) uses the Fe(II)- and α-ketoglutarate-dependent dioxygenase family of histone demethylase (represented by JmjC domain-containing histone demethylase [JHDM]); the second (type II) is for the flavin adenine dinucleotide (FAD)-dependent amine oxidase family (represented by lysine-specific demethylase 1 [LSD1]). Histone demethylase activity can then be detected by measuring the release of radiolabeled formaldehyde from ^{3}H-labeled methylated histone substrates, by monitoring the change in methylation levels of histone substrates by immunoblotting with site-specific methylhistone antibodies, or by using mass spectrometry to detect reductions in histone peptide masses that correspond to methyl groups. These assays can be applied to a wide range of histone demethylase studies, including the measurement of histone demethylase activity in tissue and cell lysates, identification of novel histone demethylases, and screening for inhibitors of histone demethylases.

RELATED INFORMATION

Based on proposed mechanisms for histone demethylation (Fig. 1), this protocol presents two different enzymatic reactions, type I and type II (data adapted from Tsukada and Zhang 2006).

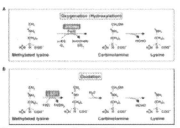

View larger version (20K):
[in this window]
[in a new window]

Figure 1. Two different mechanisms for histone demethylation. (*A*) Histone demethylation by oxygenation (hydroxylation) by JHDM family proteins, which use iron (Fe[II]) and α-ketoglutarate (α-KG) as cofactors to catalyze addition of a hydroxyl group to a methyl group on methylated lysine. This generates unstable carbinolamine and succinate, and formaldehyde is released from carbinolamine. Only monomethyl lysine is shown here, but the same mechanism can be applied to demethylate di- or trimethylated lysine residues. (*B*) Histone demethylation by oxidation catalyzed by LSD1 family proteins. LSD1 catalyzes the transfer of two hydrogen atoms from methylated lysine to FAD to form an imine intermediate. The intermediate is hydrolyzed nonenzymatically to produce unstable carbinolamine, followed by release of formaldehyde. Although only monomethyl lysine is shown, the same mechanism can be applied to dimethylated lysine residues. This mechanism cannot be used to demethylate trimethylated lysine residues because the reaction requires a protonated nitrogen on the ε-amino group of lysine.

MATERIALS

Reagents

1-Pentanol (for scintillation counting only)

α-cyano-4-hydroxycinnamic acid (10 mg/mL) (for mass spectrometry only)

Acetonitrile (ACN) (for mass spectrometry only)

Antibodies, anti-methylated-histone, site-specific (for immunoblotting only)

EDTA (2 mM) (for mass spectrometry)

Histone demethylase dialysis buffer

Histone demethylase reaction buffer (type I)

Histone demethylase reaction buffer (type II) can be used as an alternative, depending on the reaction type (see Step 3).

Histone methyltransferase (HMT), recombinant (for [^{3}H]-labeling only)

Histone octamers

Oligonucleosomes can be used as an alternative (see Step 1).

To prepare histone octamers or oligonucleosomes from HeLa cells, see Fang et al. (2004).

Histone peptides, methylated (for mass spectrometry only)

Histone storage buffer (for octamers/oligonucleosomes)

HMT reaction buffer (for [^{3}H]-labeling only)

Liquid scintillation cocktail (for scintillation counting only)

Methyl-lysine analogs (MLAs) (for immunoblotting only)

To prepare MLAs, see Simon et al. (2007).

NASH reagent (for scintillation counting only)

Protein fractions

Recombinant enzymes can be used as an alternative (see Step 2).

Reagents for SDS-PAGE (for immunoblotting only)

SDS loading buffer (5X) (for immunoblotting only)

Trichloroacetic acid (TCA) (for scintillation counting only)

Trifluoroacetic acid (TFA) (for mass spectrometry only)

Equipment

Centrifuge

Dialysis tubing

Empore extraction disk (3M) (for mass spectrometry only)

Incubators preset to 30°C, 37°C

Mass spectrometer, matrix-assisted laser-desorption/ionization time-of-flight (MALDI-TOF; e.g., Autoflex; Bruker Daltonics) (for mass spectrometry only)

Micropipettor and tips

Nitrocellulose membrane (for immunoblotting only)

Scintillation counter (for scintillation counting only)

SDS-PAGE apparatus (for immunoblotting only)

Vortex mixer

Water bath preset to 95°C (for immunoblotting only)

METHOD

Separate procedures are presented to measure enzymatic activity by scintillation counting (Steps 4-11), immunoblotting (Steps 12-15), or mass spectrometry (Steps 16-22).

In Vitro Histone Demethylation Reaction

1. Prepare the substrate:

To prepare [^{3}H]-labeled methylhistone octamers or oligonucleosomes

i. Incubate 1.5-2.0 μg of histone octamers or oligonucleosomes purified from HeLa cells with different recombinant HMTs (0.1-1.0 μg) in HMT reaction buffer for 1-2 h at 30°C.

ii. Dialyze the reaction mixtures against histone storage buffer overnight in the presence (for type II reactions) or absence (for type I reactions) of 1 mM EDTA to remove unincorporated radiolabel.
The labeled substrates are then ready for use in the demethylation reaction (see Step 3).

To prepare octamers or oligonucleosomes for immunoblotting

iii. Dialyze histone octamers or oligonucleosomes purified from HeLa cells against histone storage buffer in the presence (for type II reactions) or absence (for type I reactions) of 1 mM EDTA.

2. Dialyze the protein fractions or recombinant enzymes to be tested against histone demethylase dialysis buffer.

3. Incubate 1.5-2.0 μg of histone octamers or oligonucleosomes (with or without radiolabel, from Step 1.ii or Step 1.iii, respectively), or methylated histone peptides (0.5 μg), or MLAs (0.2-0.5 μg) with proper amount of protein fractions, or 03.3-3.0 mg of recombinant enzymes (from Step 2) in type I or type II histone demethylase reaction buffer for 1-3 h at 37°C.
Proceed to Step 4 (for scintillation counting), Step 12 (for immunoblotting), or Step 16 (for mass spectrometry), as appropriate.

Detection of Released Radioactive Formaldehyde

This procedure uses a modified NASH method (Kleeberg and Klinger 1982) to detect [^{3}H]-formaldehyde released by histone demethylation.

4. Stop the reaction (i.e., Step 3) by adding TCA to a final concentration of 12.5%. Incubate the mixture for 15 min at 4°C.
This precipitates the histone substrate and other proteins present in the reaction mixture.

5. Centrifuge the reaction at 16,000*g* for 10 min at 4°C. Remove the supernatant; measure its volume.

6. Add an equal volume of NASH reagent to the supernatant.

7. Incubate the mixture for 50 min at 37°C to convert the formaldehyde to 3,5-diacetyl-1,4-dihydrolutidine (DDL).

8. Add an equal volume of 1-pentanol to each sample. Vortex.

9. Centrifuge the reaction mixture at 16,000*g* for 3 min at room temperature to separate the DDL into the 1-pentanol phase.

10. Recover the 1-pentanol phase. Mix with liquid scintillation cocktail.

11. Analyze by scintillation counting.
Figure 2 shows the resulting histone demethylase activity of recombinant KDM7 toward various methylated histone substrates as measured by this method.

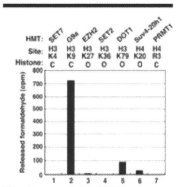

Figure 2. Histone demethylase activity of recombinant KDM7-FLAG with various methylated histone substrates, as measured by the release of radiolabeled formaldehyde. The HMTs used to generate the various substrates and their sites of methylation are indicated at the *top*. The methylated substrates were generated with the indicated forms of histone (C, core histone octamer; O, oligonucleosome) based on the substrate preference of each HMT. The counts shown are corrected for control counts.

View larger version (22K):
[in this window]
[in a new window]

Detection of Methylated Histones by Immunoblotting

12. Stop the reaction (i.e., Step 3) by adding a one-fifth volume of 5X SDS loading buffer. Incubate for 5 min at 95°C.

13. Separate the histones by SDS-PAGE on an 18% polyacrylamide gel.

14. Transfer the proteins to a nitrocellulose membrane.

15. Immunoblot with site-specific methylated histone antibodies following standard procedures.
Figure 3 shows histone demethylase activity of recombinant KDM7 toward core histone substrates as measured by this method.

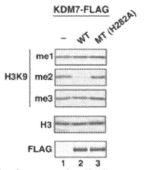

Figure 3. Immunoblot analysis of histone demethylase activity of wild-type (WT) or H282A mutant (MT) forms of recombinant KDM7-FLAG toward core histone substrates. The antibodies used are indicated to the *left*.

View larger version (24K):
[in this window]
[in a new window]

Detection of Methyl Group Release by Mass Spectrometry

16. Stop the reaction (i.e., Step 3) by adding 2 mM EDTA.

17. Dilute an aliquot of the demethylation reaction mixture 10-fold with 0.1% TFA and 2% ACN.

18. Apply the sample to an Empore extraction disk packed into a pipette tip.

19. Wash the disk with 0.1% TFA/2% ACN.

20. Elute peptides with 5 μL of 0.1% TFA/50% ACN.

21. Crystallize a fraction of the peptide pool with 10-mg/mL α-cyano-4-hydroxycinnamic acid.

22. Analyze the samples by MALDI-TOF.
Figure 4 shows the histone demethylase activity of recombinant KDM7 toward H3K9me2 and H3K9me1 peptide substrates as measured by this method.

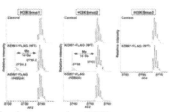

Figure 4. Mass-spectrometric analysis of the demethylase activity of wild-type (WT) or H282A mutant forms of KDM7-FLAG with methylated H3K9 peptide substrates. Numbers represent the mass-to-charge ratio of the substrate and product peptides.

View larger version (20K):
[in this window]
[in a new window]

See Troubleshooting.

TROUBLESHOOTING

Problem: There is no activity with the use of peptides.

[Step 22]

Solution: Peptides that are too short can affect recognition of the substrate by histone demethylases. Try using a longer peptide.

DISCUSSION

Until recently, histone demethylases have been elusive in part because there was no sensitive assay to detect their activity. This protocol describes two reaction conditions and three methods for measuring activity. Each of the detection methods has advantages and limitations. Measuring the release of radioactive formaldehyde from ^{3}H-labeled methylated histone substrates is the most sensitive technique, capable of detecting very low levels of activity in tissue and cell lysates. However, it is limited by the method of substrate preparation, which depends on the availability of HMTs to catalyze methylation of specific sites and statuses. Immunoblotting with site-specific methylhistone antibodies is easier to perform, but requires relatively high amounts of histone demethylase to detect activity. Because mass spectrometry uses synthesized peptides whose methylation sites and status are highly specific, this method can provide information regarding the substrate specificity of the enzyme. However, it requires the use of artificial peptides. Despite their various restrictions, the assays described here can be applied to study any demethylase that uses the same reaction mechanisms to demethylate any protein or nucleic acid.

REFERENCES

1. Fang J, Wang H, Zhang Y. 2004. Purification of histone methyltransferases from HeLa cells. *Methods Enzymol* **377:** 213–226.[Medline]
2. Kleeberg U, Klinger W. 1982. Sensitive formaldehyde determination with Nash's reagent and a 'tryptophan reaction'. *J Pharmacol Methods* **8:** 19–31.[Medline]
3. Simon MD, Chu F, Racki LR, de la Cruz CC, Burlingame AL, Panning B, Narlikar GJ, Shokat KM. 2007. The site-specific installation of methyl-lysine analogs into recombinant histones. *Cell* **128:** 1003–1012.[Medline]
4. Tsukada Y, Zhang Y. 2006. Purification of histone demethylases from HeLa cells. *Methods* **40:** 318–326.[Medline]

Caution

1-Pentanol

1-Pentanol is highly flammable in liquid and vapor forms and is toxic. It is harmful by inhalation, ingestion, or skin absorption. Wear appropriate gloves and safety glasses and use in a chemical fume hood. Keep away from heat, sparks, and open flame.

Caution

α-Cyano-4-hydroxycinnamic acid (CHCA)

α-Cyano-4-hydroxycinnamic acid (CHCA) may cause cardiac disturbances. Chronic effects may be delayed. It may be harmful by inhalation, ingestion, or skin absorption. Wear appropriate gloves and safety glasses.

Caution

Acetonitrile

Acetonitrile is very volatile and extremely flammable. It is an irritant and a chemical asphyxiant that can exert its effects by inhalation, ingestion, or skin absorption. Treat cases of severe exposure as cyanide poisoning. Wear appropriate gloves and safety glasses. Use only in a chemical fume hood. Keep away from heat, sparks, and open flame.

Caution

Trichloroacetic acid (TCA)

Trichloroacetic acid (TCA) is highly caustic. Wear appropriate gloves and safety goggles.

Caution

Trifluoroacetic acid (TFA)

Trifluoroacetic acid (TFA) may be harmful by inhalation, ingestion, or skin absorption. Concentrated acids must be handled with great care. Decomposition causes toxic fumes. Wear appropriate gloves and a face mask. Use in a chemical fume hood.

Recipe

EDTA

EDTA (ethylenediamenetetraacetic acid)

NaOH

To prepare EDTA at 0.5 M (pH 8.0): Add 186.1 g of disodium EDTA•2H_2O to 800 mL of H_2O. Stir vigorously on a magnetic stirrer. Adjust the pH to 8.0 with NaOH (~20 g of NaOH pellets). Adjust the volume to 1 L with H_2O. Dispense into aliquots and sterilize by autoclaving. The disodium salt of EDTA will not go into solution until the pH of the solution is adjusted to ~8.0 by the addition of NaOH.

Recipe

HMT reaction buffer

S-Adenosyl-L-[methyl-^{3}H] methionine (0.03 mCi/mL; PerkinElmer)

DTT (dithiothreitol; 0.5 mM)

EDTA (4 mM)

PMSF (phenylmethylsulfonyl fluoride; 1 mM)

Tris-Cl (20 mM, pH 8.0)

Recipe

Histone demethylase dialysis buffer

Aprotinin (1 mg/mL)

DTT (dithiothreitol; 1 mM)

Glycerol (10%)

HEPES-KOH (40 mM, pH 7.9)

KCl (50 mM)

Leupeptin (1 mg/mL)

Pepstatin A (1 mg/mL)

PMSF (phenylmethylsulfonyl fluoride; 0.2 mM)

For Type II reactions, add 0.2 mM EDTA.

Recipe

Histone demethylase reaction buffer (type I)

α-ketoglutarate (1 mM)

Ascorbate (2 mM)

Ammonium ferrous sulfate ($Fe[NH_4]_2[SO_4]_2$; 7-700 μM)

HEPES-KOH (50 mM, pH 8.0)

Recipe

Histone demethylase reaction buffer (type II)

Glycine (100 mM, pH 8.0)

KCl (50 mM)

Recipe

Histone storage buffer

Glycerol (10%)

HEPES-KOH (10 mM, pH 7.5)

KCl (10 mM)

PMSF (phenylmethylsulfonyl fluoride; 0.2 mM)

For Type II reactions, add 1 mM EDTA.

Recipe

NASH reagent

2,4-pentanedione (0.2%)

Acetic acid (0.1 M)

Ammonium acetate (3.89 M)

Recipe

SDS loading buffer (5X)

- Bromophenol blue (0.25%)
- DTT (dithiothreitol; 0.5 M)

Glycerol (50%)

- SDS (sodium dodecyl sulfate; 10%)
- Tris-Cl (0.25 M, pH 6.8)

LETTER

doi:10.1038/nature09732

SCF^{FBW7} regulates cellular apoptosis by targeting MCL1 for ubiquitylation and destruction

Hiroyuki Inuzuka[1], Shavali Shaik[1]*, Ichiro Onoyama[2]*, Daming Gao[1], Alan Tseng[1], Richard S. Maser[3,4], Bo Zhai[5], Lixin Wan[1], Alejandro Gutierrez[6], Alan W. Lau[1], Yonghong Xiao[3], Amanda L. Christie[6,7], Jon Aster[8], Jeffrey Settleman[9], Steven P. Gygi[5], Andrew L. Kung[6,7], Thomas Look[6], Keiichi I. Nakayama[2], Ronald A. DePinho[3] & Wenyi Wei[1]

The effective use of targeted therapy is highly dependent on the identification of responder patient populations. Loss of *FBW7*, which encodes a tumour-suppressor protein, is frequently found in various types of human cancer, including breast cancer, colon cancer[1] and T-cell acute lymphoblastic leukaemia (T-ALL)[2]. In line with these genomic data, engineered deletion of *Fbw7* in mouse T cells results in T-ALL[3–5], validating FBW7 as a T-ALL tumour suppressor. Determining the precise molecular mechanisms by which FBW7 exerts antitumour activity is an area of intensive investigation. These mechanisms are thought to relate in part to FBW7-mediated destruction of key proteins relevant to cancer, including Jun[6], Myc[7], cyclin E[8] and notch 1 (ref. 9), all of which have oncoprotein activity and are overexpressed in various human cancers, including leukaemia. In addition to accelerating cell growth[10], overexpression of Jun, Myc or notch 1 can also induce programmed cell death[11]. Thus, considerable uncertainty surrounds how FBW7-deficient cells evade cell death in the setting of upregulated Jun, Myc and/or notch 1. Here we show that the E3 ubiquitin ligase SCF^{FBW7} (a SKP1–cullin-1–F-box complex that contains FBW7 as the F-box protein) governs cellular apoptosis by targeting MCL1, a pro-survival BCL2 family member, for ubiquitylation and destruction in a manner that depends on phosphorylation by glycogen synthase kinase 3. Human T-ALL cell lines showed a close relationship between *FBW7* loss and MCL1 overexpression. Correspondingly, T-ALL cell lines with defective FBW7 are particularly sensitive to the multi-kinase inhibitor sorafenib but resistant to the BCL2 antagonist ABT-737. On the genetic level, *FBW7* reconstitution or *MCL1* depletion restores sensitivity to ABT-737, establishing MCL1 as a therapeutically relevant bypass survival mechanism that enables *FBW7*-deficient cells to evade apoptosis. Therefore, our work provides insight into the molecular mechanism of direct tumour suppression by FBW7 and has implications for the targeted treatment of patients with *FBW7*-deficient T-ALL.

MCL1 is frequently overexpressed in various leukaemias through mechanisms that are not fully understood[12]. MCL1 is distinct from other BCL2 family members in its extremely unstable nature[13], which provides a mechanism for cells to switch to either survival or apoptotic mode in response to various stresses[14]. Phosphorylation of MCL1 by glycogen synthase kinase 3 (GSK3) regulates the stability of MCL1 (ref. 13), but little is known about the identity of the E3 ubiquitin ligase that targets phosphorylated MCL1 for destruction. On examination of the GSK3-mediated phosphorylation sites in MCL1, we surmised that they resemble a degron sequence that can be recognized by FBW7 (also known as FBXW7) (Fig. 1a), prompting us to test the possibility that GSK3-mediated phosphorylation of MCL1 triggers the degradation of MCL1 by FBW7. Depletion of FBW7 (Fig. 1b) or the SCF components cullin 1 (CUL1), RBX1 and SKP1 (Fig. 1c), but not other F-box proteins that we examined (Fig. 1b), resulted in a significant increase in the amount of MCL1 protein. T-cell-lineage-specific depletion of FBW7 in *Fbw7* conditional knockout (Lck-Cre/$Fbw7^{fl/fl}$)mice[3] resulted in increased MCL1 levels in the thymuses of these mice (Fig. 1d), as well as thymic lymphoma (Supplementary Fig. 1a) and the presence of acute leukaemia cells in the thymuses (Supplementary Fig. 1b). Consistent with a recent study[15], $FBW7^{-/-}$ human DLD1 cells (Fig. 1e) and HeLa cells treated with short interfering RNA (siRNA) directed against *FBW7* (Supplementary Fig. 1c) have elevated MCL1 expression mainly in the mitosis (M) and early G1 phases of the cell cycle.

The clinical relevance of this finding is further demonstrated by the finding that human T-ALL cell lines harbouring *FBW7* mutations and/or deletions have a significant increase in MCL1 (Fig. 1f). Additionally, depletion of FBW7 in DND41 cells or Loucy cells (both of which have wild-type *FBW7*) leads to increased MCL1 expression (Fig. 1g), whereas reintroduction of wild-type *FBW7* dramatically reduced MCL1 expression in FBW7-deficient T-ALL cells (Fig. 1h), supporting a causal relationship between loss of FBW7 activity and elevated MCL1 expression in the T-ALL cells examined. More importantly, elevated MCL1 expression is also observed in both primary human and mouse T-ALL samples with deficient FBW7 activity[2–4] (Fig. 1i, j and Supplementary Fig. 1a, b), and depletion of MCL1 impaired T-ALL disease progression *in vivo* (Fig. 1k–m).

Consistent with a post-translational mode of regulation, no changes in *MCL1* mRNA levels were observed after depletion of FBW7 in DLD1 cells (Supplementary Fig. 2d), and no positive relationship was observed between *MCL1* mRNA levels and loss of *FBW7* in T-ALL cells (Supplementary Fig. 2e). The half-life of MCL1 was significantly extended in the thymuses of $Fbw7^{-/-}$ mice and FBW7-deficient human T-ALL cells (Supplementary Fig. 3a–c), and experimental manipulation of FBW7 levels changed MCL1 stability accordingly (Supplementary Fig. 3d, e). Together, these results suggest that MCL1 is a downstream ubiquitylation target of SCF^{FBW7}.

As the proper substrate phosphorylation events are required for FBW7 to recognize and target its substrates for ubiquitylation[16], we next investigated which phosphorylation events trigger MCL1 destruction by FBW7. Mass spectrometry analysis showed that MCL1 is phosphorylated at multiple sites *in vivo* (Fig. 2a and Supplementary Fig. 5a–c). In addition to serine at position 159 (S159) and threonine at position 163 (T163)[13,17], S64 and S121 were also phosphorylated *in vivo*. Consistent with previous reports[13,17], MCL1 destruction is promoted by GSK3 (Fig. 2b) but not by the protein kinases ERK1 (also

[1]Department of Pathology, Beth Israel Deaconess Medical Center, Harvard Medical School, 330 Brookline Avenue, Boston, Massachusetts 02215, USA. [2]Department of Molecular and Cellular Biology, Medical Institute of Bioregulation, Kyushu University, Fukuoka, Fukuoka 812-8582, Japan. [3]Belfer Institute for Applied Cancer Science, Department of Medical Oncology, Dana-Farber Cancer Institute, Harvard Medical School, Boston, Massachusetts 02115, USA. [4]The Jackson Laboratory, Bar Harbor, Maine 04609, USA. [5]Department of Cell Biology, Harvard Medical School, Boston, Massachusetts 02115, USA. [6]Department of Pediatric Oncology, Dana-Farber Cancer Institute, Harvard Medical School, Boston, Massachusetts 02115, USA. [7]Lurie Family Imaging Center, Dana-Farber Cancer Institute, Boston, Massachusetts 02115, USA. [8]Department of Pathology, Brigham and Women's Hospital, Harvard Medical School, Boston, Massachusetts 02115, USA. [9]Department of Medicine, Massachusetts General Hospital Cancer Center, Harvard Medical School, Charlestown, Massachusetts 02129, USA.
*These authors contributed equally to this work.

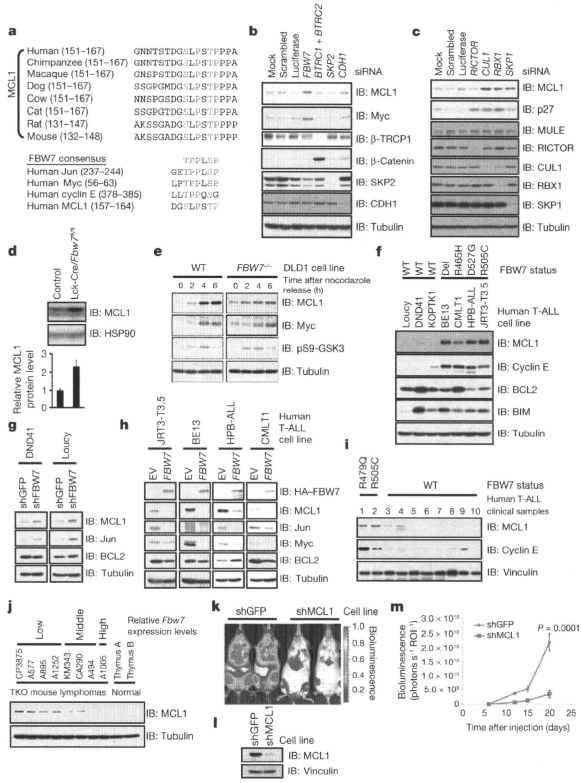

Figure 1 | MCL1 stability is controlled by FBW7. **a**, Sequence alignment of MCL1 with the phosphodegron sequences recognized by FBW7 in Jun, Myc and cyclin E. The putative FBW7 phosphodegron sequence present in MCL1 is conserved across different species. Conserved serine and threonine residues within the degron sequences are shown in red, and conserved proline residues are shown in blue. **b**, **c**, Immunoblotting (IB) analysis, with antibodies specific for the indicated proteins (right), of HeLa cells transfected with siRNA oligonucleotides directed against the indicated genes (top). **d**, IB analysis of thymocytes derived from control (Lck-Cre/$Fbw7^{+/fl}$) mice or *Fbw7* conditional knockout (Lck-Cre/$Fbw7^{fl/fl}$) mice (whose thymocytes lack *Fbw7*). For the histogram, MCL1 band intensity was normalized to HSP90 and then normalized to the control lane. Data are shown as mean ± s.e.m. for three independent experiments. **e**, IB analysis of wild-type (WT) and $FBW7^{-/-}$ DLD1 cells after synchronization of the cell cycles with nocodazole and release from mitotic arrest at the indicated time points. pS9-GSK3, GSK3 that is phosphorylated at the S9 residue. **f**, IB analysis of the indicated human T-ALL cell lines, which have either WT FBW7 or mutant FBW7 (a deletion (Del) or an amino acid substitution). **g**, The human T-ALL cell lines DND41 and Loucy cells, which contain wild-type *FBW7*, were infected with the indicated lentiviral shRNA constructs and selected with 1 μg ml^{-1} puromycin to eliminate the non-infected cells. Cell lysates were collected for IB analysis. shFBW7, shRNA specific for *FBW7*; shGFP, shRNA specific for the gene encoding green fluorescent protein (GFP). **h**, Human T-ALL cell lines deficient in FBW7 were infected with an *FBW7*-expressing retroviral construct (with empty vector (EV) as a negative control) and selected with 1 μg ml^{-1} puromycin to eliminate the non-infected cells. Cell lysates were collected for IB analysis. HA, haemagglutinin tag. **i**, IB analysis of the indicated primary human T-ALL clinical samples. **j**, IB analysis of the indicated mouse T-ALL cell lines derived from $Terc^{-/-}Atm^{-/-}Tp53^{-/-}$ (TKO) mice. **k**–**m**, *In vivo* effects of MCL1 depletion in FBW7-deficient T-ALL cells. An *in vivo* model of FBW7-deficient T-ALL was created by orthotopic engraftment of luciferase-expressing CMLT1 cells in immunodeficient (NOD SCID *Il2rg*-null) mice. Mice were injected with 1×10^7 cells ($n = 7$ per group) through the lateral tail vein. Before engraftment, cells were infected with retroviral constructs expressing the indicated shRNAs. **k**, Representative images of luciferase expression (photonic flux, in number of photons s^{-1} cm^{-2} sr^{-1} × 10^6) detected in live mice, which had received CMLT1–shGFP (left) or CMLT1–shMCL1 (right). **l**, IB analysis of the engineered CMLT1 cell lines, showing the efficient depletion of MCL1. **m**, Tumour burden was determined by quantification of total body luminescence and is expressed as photons s^{-1} ROI^{-1}. Data are presented as mean ± s.e.m., with statistical significance determined by Student's *t*-test.

known as MAPK3) and/or ERK2 (also known as MAPK1) (Supplementary Fig. 5d–f). To investigate further the significance of each individual phosphorylation site, we created a panel of MCL1 mutants (Fig. 2c). Using *in vitro* kinase assays, we identified S159 and T163 as the major GSK3-mediated phosphorylation sites[17] and S121 as a minor GSK3-mediated phosphorylation site (Fig. 2d, e and Supplementary

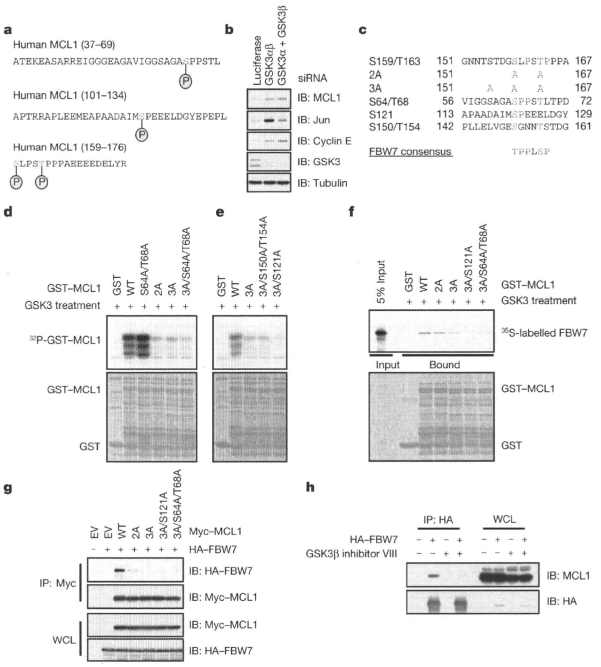

Figure 2 | Phosphorylation of MCL1 by GSK3 triggers the interaction of MCL1 with FBW7. **a**, *In vivo* MCL1 phosphorylation sites detected by mass spectrometry analysis. Phosphorylated residues are shown in red, with phosphate in blue. **b**, IB analysis, with antibodies specific for the indicated proteins (right), of HeLa cells transfected with siRNA oligonucleotides directed against the indicated genes (top) (where GSK3αβ indicates depletion of *GSK3A* and *GSK3B* with a single siRNA and GSK3α + GSK3β indicates depletion with siRNAs targeting each gene separately). **c**, Illustration of the various MCL1 mutants generated for this study. Conserved serine and threonine residues within the degron sequence are shown in red, and conserved proline residues are shown in blue. 2A, MCL1 S159A/T163A; 3A, MCL1 S155A/S159A/T163A. **d**, **e**, GSK3 phosphorylates MCL1 *in vitro* at multiple sites. Purified GSK3 protein was incubated with 5 μg of the indicated glutathione *S*-transferase (GST)–MCL1 fusion proteins (top, WT and mutant as in **c**) in the presence of [γ-^{32}P]ATP. The protein kinase reaction products were resolved by SDS–PAGE, and phosphorylation was detected by autoradiography. **f**, Phosphorylation of MCL1 at multiple sites by GSK3 triggers the interaction of MCL1 with FBW7 *in vitro*. Autoradiograms show recovery of ^{35}S-labelled FBW7 protein bound to the indicated GST–MCL1 fusion proteins (with GST protein as a negative control) incubated with GSK3 before the pull-down assays. **g**, IB analysis of whole-cell lysates (WCL) and immunoprecipitates (IP) derived from 293T cells transfected with HA–FBW7 together with the indicated Myc–MCL1 constructs (top). Thirty hours after transfection, cells were pretreated with 10 μM MG132 for 10 h to block the proteasome pathway before cell collection. **h**, IB analysis of WCL and IP derived from 293T cells transfected with HA–FBW7. Thirty hours after transfection, cells were pretreated with 20 μM MG132 for 8 h to block the proteasome pathway before cell collection. Where indicated, 25 μM GSK3β inhibitor VIII (with dimethylsulphoxide (DMSO) as a negative control) was added for 8 h before cell collection.

Fig. 5g). Inactivation of these GSK3-mediated phosphorylation sites impairs the interaction between MCL1 and FBW7 both *in vitro* (Fig. 2f and Supplementary Fig. 5h) and *in vivo* (Fig. 2g and Supplementary Fig. 5i). Furthermore, pharmacological inhibition of GSK3 activity blocked the interaction between HA-tagged FBW7 and endogenous MCL1 (Fig. 2h) and inhibited the localization of FBW7 to the mitochondria, where MCL1 resides (Supplementary Fig. 5j, k). These results indicate that GSK3-dependent phosphorylation of MCL1 is necessary for the interaction of MCL1 with FBW7. Consistent with this FBW7–MCL1 regulatory axis, MCL1 specifically interacts with FBW7 (Supplementary Fig. 6a, b, j–l) and CUL1 (Supplementary Fig. 6c, d), and depletion of endogenous CUL1 increases MCL1 abundance (Supplementary Fig. 11a).

We next explored the mechanism by which FBW7 alters MCL1 stability. Overexpression of FBW7 and GSK3 significantly decreased MCL1 abundance (Fig. 3a and Supplementary Fig. 6h), whereas inactivation of the major GSK3-dependent phosphorylation sites on MCL1 impaired FBW7-mediated destruction (Fig. 3b and Supplementary Fig. 6e–g). All FBW7 isoforms (particularly the α-isoform and the γ-isoform) participate in MCL1 stability control, and FBW7 dimerization is not required for the degradation of MCL1 (Supplementary Fig. 7a–e). Mutant FBW7 constructs derived from patients with T-ALL showed a reduced ability to interact with MCL1 (Supplementary Fig. 6i) and were therefore unable to degrade MCL1 (Fig. 3c). Moreover, the FBW7- and GSK3-mediated destruction of MCL1 was blocked by the proteasome inhibitor MG132, indicating the involvement of the ubiquitin–proteasome pathway in this process (Fig. 3a). In support of this idea, co-expression of GSK3 and FBW7 resulted in a marked reduction in the half-life of wild-type MCL1, but not of the 2A or 3A MCL1 mutants (Fig. 3d), with reduced interaction with FBW7

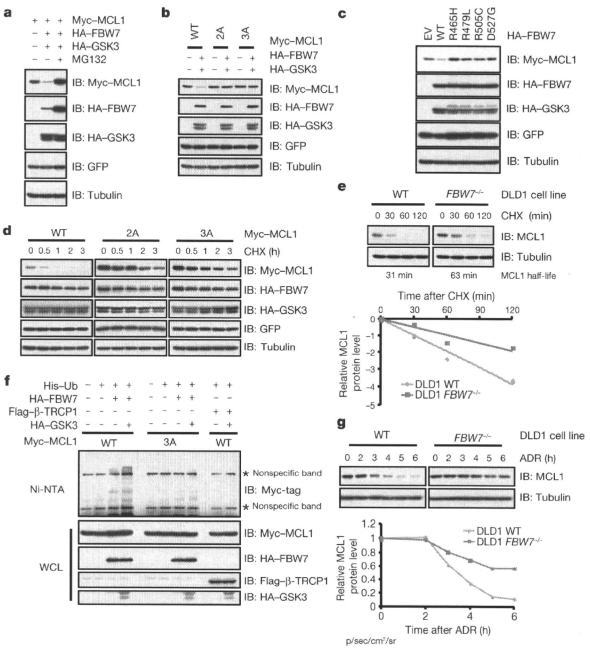

Figure 3 | FBW7 promotes MCL1 ubiquitylation and destruction in a GSK3-mediated phosphorylation-dependent manner. **a**–**c**, GSK3-mediated phosphorylation-dependent degradation of MCL1 by FBW7. IB analysis of 293T cells transfected with plasmids expressing the indicated Myc–MCL1 and HA–FBW7 proteins in the presence or absence of HA–GSK3 (top), with antibodies specific for the Myc tag, HA tag, GFP or tubulin (right). A plasmid encoding GFP was used as a negative control for transfection efficiency. Where indicated, the proteasome inhibitor MG132 was added. **d**, 293T cells were transfected with the indicated Myc–MCL1 constructs together with the HA–FBW7- and HA–GSK3-expressing plasmids. Twenty hours after transfection, cells were split into 60-mm dishes. After another 20 h, cells were treated with 20 μg ml^{-1} cycloheximide (CHX). At the indicated time points, WCL were prepared, and IB analysis was carried out with antibodies specific for the indicated proteins. **e**, Top, WT or *FBW7*$^{-/-}$ DLD1 cells were treated with 20 μg ml^{-1} CHX. At the indicated time points, WCL were prepared, and IB analysis was carried out with antibodies specific for the indicated proteins. Bottom, MCL1 band intensity was normalized to tubulin and then normalized to the $t = 0$ controls. **f**, IB of WCL and His tag pull-down of HeLa cells transfected with plasmids expressing the indicated proteins. Twenty hours after transfection, cells were treated with the proteasome inhibitor MG132 for 12 h before cell collection. His tag pull-down was performed in the presence of 8 M urea to eliminate any possible contamination from MCL1-associated proteins. Ni-NTA, nickel-nitrilotriacetic acid; Ub, ubiquitin. **g**, Top, IB analysis of WT and *FBW7*$^{-/-}$ DLD1 cells treated with 10 μM adriamycin (ADR) for the indicated time durations. Bottom, MCL1 band intensity was normalized to tubulin and then normalized to the $t = 0$ controls.

(Fig. 2g). Furthermore, loss of *FBW7* extends the half-life of endogenous MCL1 (Fig. 3e), and FBW7 promotes the ubiquitylation of MCL1 in a GSK3-dependent manner (Fig. 3f and Supplementary Fig. 8a, b, e). The decrease of MCL1 expression is also impaired in response to various DNA-damaging agents[18] in *FBW7*$^{-/-}$ DLD1 cells (Fig. 3g and Supplementary Fig. 8f). Together, these data suggest a physiological role for FBW7 in promoting MCL1 destruction *in vivo* in a GSK3-mediated phosphorylation-dependent manner.

Next, we explored how FBW7 affects the cellular apoptotic response by modulating MCL1 abundance. As predicted, *Fbw7*$^{-/-}$ mouse thymocytes and FBW7-deficient human T-ALL cells with increased MCL1 levels were less sensitive to apoptotic stimuli (Supplementary Fig. 9a–f). More interestingly, compared with T-ALL cell lines that had wild-type *FBW7*, FBW7-deficient T-ALL cells with elevated MCL1 expression (Fig. 1f and Supplementary Fig. 9h) were more sensitive to the multi-kinase inhibitor sorafenib, which can effectively reduce MCL1 expression[19,20] (Fig. 4a and Supplementary Fig. 9g–i). Although the ability of sorafenib to repress MCL1 has been attributed to the inactivation of the RAF–ERK pathway and/or the activation of GSK3 activity[19], the exact mechanism remains unclear. Nonetheless, these data suggest that FBW7-deficient T-ALL cell lines might require elevated levels of MCL1 to evade apoptosis, a phenotype known as 'oncogene addiction'[21]. By contrast, FBW7-deficient T-ALL cell lines were more resistant to ABT-737 (Fig. 4a and Supplementary Fig. 9g, j). ABT-737 is a BH3 domain mimetic and a pan inhibitor of the BCL2 family of anti-apoptotic proteins, and it is reported to kill leukaemia cells effectively[22]. However, leukaemia cells with elevated MCL1 levels are refractory to treatment with ABT-737 (refs 23, 24), primarily because ABT-737 fails to inactivate MCL1 (ref. 22). Experimental evidence from both double staining with 7-amino-actinomycin D (7-AAD) and annexin V (Supplementary Fig. 9j) and immunoblotting specific for apoptotic biomarkers (Fig. 4b) suggests that ABT-737-induced apoptosis is impaired in FBW7-deficient T-ALL cells. Moreover, specific depletion of MCL1 in multiple FBW7-deficient T-ALL cell lines restored the sensitivity of these cells to ABT-737 (Fig. 4c, d), supporting the idea that increased MCL1 expression is

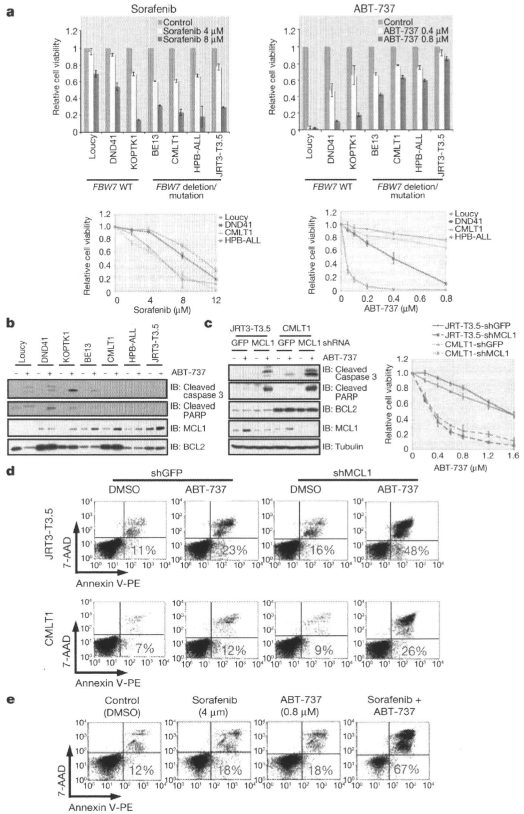

Figure 4 | Elevated MCL1 expression protects FBW7-deficient T-ALL cell lines from ABT-737-induced apoptosis. **a**, Cell viability assays showing that FBW7-deficient human T-ALL cell lines were more sensitive to sorafenib but were relatively resistant to ABT-737 treatment. T-ALL cells were cultured in 10% FBS-containing medium with the indicated concentrations of sorafenib or ABT-737 for 48 h before cell viability assays were performed. Data are shown as mean ± s.d. for three independent experiments. **b**, IB analysis of the indicated human T-ALL cell lines with or without ABT-737 (0.8 μM) treatment. PARP, poly(ADP-ribose) polymerase. **c**, Specific depletion of endogenous MCL1 expression restored sensitivity to ABT-737 in the indicated FBW7-deficient human T-ALL cell lines. Various T-ALL cell lines were infected with lentiviral shGFP- or shMCL1-encoding vectors and selected in 0.5 μg ml^{-1} puromycin to eliminate non-infected cells. The generated cell lines were cultured in 10% FBS-containing medium with the indicated concentrations of ABT-737 for 48 h before cell viability assays were performed (right) or with or without ABT-737 (0.8 μM) treatment for 24 h before WCL were collected for IB analysis with antibodies specific for the indicated proteins (left). For cell viability assays, data are shown as mean ± s.d. for three independent experiments. **d**, Double staining with 7-AAD and annexin-V–PE (annexin V conjugated to phycoerythrin), followed by flow cytometry analysis to detect the percentage of apoptotic cells (axes indicate intensity of fluorochrome). In the indicated FBW7-deficient human T-ALL cell lines, endogenous MCL1 was depleted by infection with lentiviral vectors encoding shRNA (lentiviral shGFP was used as a negative control). Cell lines were cultured in 10% FBS-containing medium with or without ABT-737 (0.8 μM) treatment, with DMSO as a negative control, for 48 h before the flow cytometry analysis. Purple numbers indicate the percentage of apoptotic cells. **e**, Staining and flow cytometry analysis as in **d**, demonstrating that sorafenib treatment restores ABT-737 sensitivity to FBW7-deficient HPB-ALL cells. HPB-ALL cells were cultured in 10% FBS-containing medium with the indicated concentrations of sorafenib and/or ABT-737 for 48 h before analysis. Coloured numbers indicate the percentage of apoptotic cells.

the primary cause of desensitization to ABT-737 *in vivo*[23,24]. It also suggests that patients with FBW7-deficient T-ALL will not respond well to treatment with ABT-737. We further demonstrated that manipulation of FBW7 activity or ectopic expression of a non-degradable form of MCL1 in human T-ALL cells affects their sensitivity to ABT-737 (Supplementary Fig. 10a, b) and responses to other apoptotic stimuli (Supplementary Fig. 10c–f).

Our results indicate that inhibition of MCL1 could be used to restore sensitivity to ABT-737 in FBW7-deficient T-ALL cells. Given that the clinical application of siRNA- or short hairpin RNA (shRNA)-mediated target extinction is not yet feasible owing to delivery challenges, we instead exploited small molecule strategies to reduce MCL1 expression, specifically with the use of sorafenib (Supplementary Fig. 9h). The combined use of sorafenib and ABT-737 produced a dose-dependent